# An electrostatic levitator for high-temperature containerless materials processing in 1-g

Won-Kyu Rhim, Sang K. Chung, Daniel Barber, Kin F. Man, Gary Gutt, Aaron Rulison,[a] and R. Erik Spjut[b]
*Jet Propulsion Laboratory, California Institute of Technology, 4800 Oak Grove Drive, Pasadena, California 91109*

This article discusses recent developments in high-temperature electrostatic levitation technology for containerless processing of metals and alloys. Presented is the first demonstration of an electrostatic levitation technology which can levitate metals and alloys (2–4 mm diam spheres) in vacuum and of superheating-undercooling-recalescence cycles which can be repeated while maintaining good positioning stability. The electrostatic levitator (ESL) has several important advantages over the electromagnetic levitator. Most important is the wide range of sample temperature which can be achieved without affecting levitation. This article also describes the general architecture of the levitator, electrode design, position control hardware and software, sample heating, charging, and preparation methods, and operational procedures. Particular emphasis is given to sample charging by photoelectric and thermionic emission. While this ESL is more oriented toward ground-based operation, an extension to microgravity applications is also addressed briefly. The system performance was demonstrated by showing multiple superheating-undercooling-recalescence cycles in a zirconium sample ($T_m = 2128$ K). This levitator, when fully matured, will be a valuable tool both in Earth-based and space-based laboratories for the study of thermophysical properties of undercooled liquids, nucleation kinetics, the creation of metastable phases, and access to a wide range of materials with novel properties.

## I. INTRODUCTION

A capability for containerless materials processing is important for the study of thermophysical properties of undercooled liquid states, nucleation kinetics, and for the production of various metastable phases with novel properties in different materials. The electrostatic levitator described in this article provides the capability of superheating, undercooling, and solidifying metals and alloys in a clean (contactless and high vacuum) and quiescent environment. This levitator is an extension of the one previously described[1] in which sample levitation was limited to low density materials at ambient conditions.

Suspension of charged particles by electrostatic forces has a rather long history.[2-4] To our knowledge, however, none of these past applications have addressed high-temperature materials processing of large samples. The advantages of the present high-temperature high-vacuum electrostatic levitator (ESL) when compared with the electromagnetic levitator (EML)[5] are (i) The ESL can accommodate a broad range of materials, including metals, semiconductors, and insulators, since maintaining a sufficient surface charge on the sample is the only requirement to generate a levitation force. In contrast, an EML relies on eddy currents induced in a conducting sample by an applied rf magnetic field. Mutual interaction between the eddy currents and the applied field results in a levitation force. Materials that the EML can levitate are, therefore, limited primarily to electrical conductors. (ii) In an ESL, sample heating and levitation do not interfere with each other so that the sample temperature can be varied over a wide range, whereas the electromagnetic field in an EML is intrinsically coupled to sample heating, which limits the lowest temperature it can attain for a given sample density. (iii) The ESL, through employment of feedback control, provides quiescent positioning during sample processing, whereas a molten sample levitated by an EML is subjected to strong internal flow which may cause severe shape distortion, prevents accurate temperature measurements, and perhaps causes premature nucleation, therefore preventing deeper undercooling. (iv) The ESL provides a more open view, whereas the levitation and heating coils in an EML are closely wound around the levitated sample, severely restricting access to the diagnostic instruments. However, one major drawback of the ESL is that it requires either a high-vacuum or a high-pressure environment in order for a high electric field to be applied without causing gas breakdown.

We describe in this article an electrostatic levitator which has demonstrated for the first time the capability to process materials at high temperature in a clean environment. A brief review of the basic principles of an electrostatic levitator is given, followed by a description of the general architecture of the levitator, electrode design, position control hardware and software, sample heating, charging, and the operational procedures. The system performance is demonstrated using zirconium samples which melt at 2128 K. We conclude with a discussion on some intrinsic problems and aspects that need to be improved in

[a] NASA-NRC Resident Research Associate.
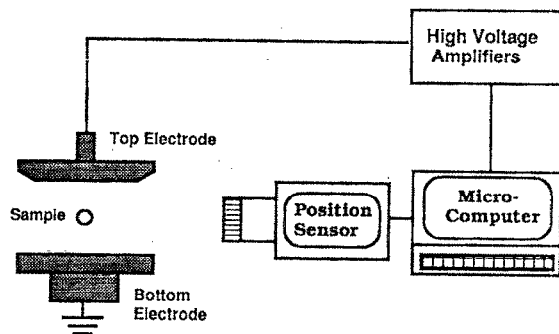[b] Department of Engineering, Harvey Mudd College, Claremont, CA.

FIG. 1. Schematic diagram of an electrostatic levitator in which the sample position is actively controlled only along the vertical direction. It relies on a two-dimensional potential well for centering in the lateral direction.

the future, and also point out how some of the difficulties we face in ground-based laboratories can be overcome in the microgravity environment of space.

## II. THE PRINCIPLES OF ELECTROSTATIC LEVITATION

In electrostatic levitation the positioning of a charged sample is achieved through the application of feedback-controlled electrostatic fields that are generated by a set of appropriately positioned electrodes around the sample. Since a three-dimensional electrostatic potential minimum does not exist (Earnshaw's theorem[6]), electrostatic sample positioning is only possible with an actively controlled applied electric field. Our system uses a feedback control to correct any deviation in sample position from a preset position.

Figure 1 is a schematic diagram of an electrostatic levitator with one-dimensional control capability. This system employs single-axis position control along the vertical direction to overcome the gravitational force, $mg$. The vertical position information from a position detector is compared to a preset $z$ coordinate to generate an error signal which is processed by a computer to generate a control signal according to a feedback algorithm. The control signal is amplified and applied to the top electrode to maintain the sample at the preset position. The force-balance equation for levitation when the sample is positioned at the center of a pair of infinite parallel electrodes is given approximately by

$$mg = Q_s V/L, \qquad (1)$$

where $m$ is the mass of the sample carrying a charge $Q_s$, and $V$ is the voltage difference between the two electrodes separated by a distance $L$. For $Q_s = 0.69 \times 10^{-9}$ C, $m = 140$ mg, and $L = 10$ mm, $V$ is approximately $-10$ kV.

As explained elsewhere,[7] the electrode arrangement shown in Fig. 1 provides a two-dimensional potential well in the horizontal direction when it is operated in the presence of a gravitational force on Earth. In the microgravity environment of space a different electrode arrangement and control method would be required.
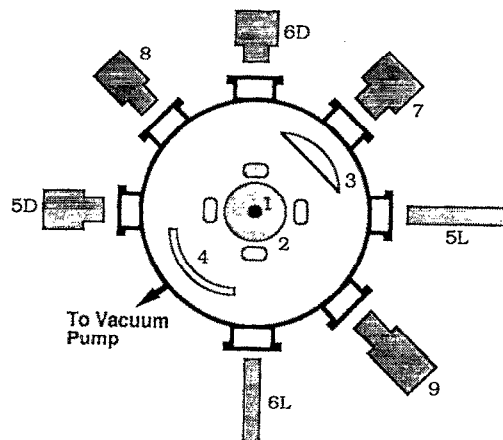


FIG. 2. Schematic diagram of the high-temperature high-vacuum electrostatic levitator designed for ground-based applications. 1 is the sample, 2 is the electrode assembly, 3 is the focusing lens, 4 is the spherical reflector, 5D and 6D are the position detectors, 5L and 6L are the He-Ne lasers, 7 is the 1 kW xenon lamp, 8 is the video camera with a telephoto lens, and 9 is the pyrometer.

## III. THE EXPERIMENTAL HARDWARE

A schematic diagram of the present high-temperature/high-vacuum electrostatic levitator is shown in Fig. 2. The electrode assembly is housed in a cylindrical vacuum chamber and all the necessary equipment for levitation, heating, and diagnostics are located around the chamber. The 30 $\ell$ stainless steel chamber can be evacuated to an ultimate vacuum of $5 \times 10^{-8}$ Torr by a vibration-free magnetically suspended turbomolecular pump (Osaka model TH250M) backed by a roughing pump (Danielson model TD100).

The electrode assembly shown schematically in Fig. 3 is located at the center of the chamber. The basic difference between this and the assembly shown in Fig. 1 is the addition of two pairs of side electrodes surrounding the bottom electrode. Damping voltages applied on these side electrodes prevent sample oscillation in the lateral direc-
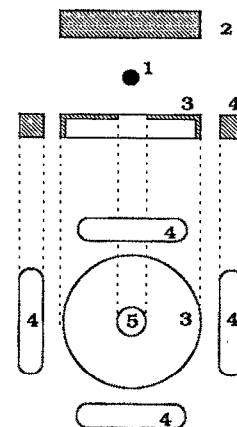


FIG. 3. Schematic diagram of the electrode assembly (side and top views), where 1 is the sample, 2 is the top electrode, 3 is the bottom electrode, 4's are the side electrodes, and 5 is the hole which allows access to the sample storage system.

tions. Without the side electrodes the lateral position instability would introduce uncertainties into the diagnostic measurements.

Two orthogonal HeNe lasers (30 mW each) together with two position detectors provide the three-dimensional position information which is used by the microcomputer to generate a feedback signal. A Macintosh IIfx computer and 12 bit Analog to Digital (A/D) and Digital to Analog (D/A) converter cards were used for data acquisition and position control. The computer is equipped with a Motorola 50 MHz 68030 microprocessor and 68882 floating point math coprocessor. The 12 bit A/D and D/A cards from National Instruments fit into the Nubus inside the computer. The three position signals (produced by the two orthogonally positioned detectors) are fed into the computer through an A/D card, and after going through the control routine the three output signals are sent to the high-voltage amplifiers through a D/A card. The position sensitive detectors (PSD cameras by HAMAMATSU, model C2399-01) are commercially available. This type of detector is normally used for sensing a bright image on a dark background. In this system, however, due to the xenon lamp light (used for heating) which brightly illuminates the chamber and the sample, they are being used in a reversed mode (dark image on a bright background). The sample is backlit by collimated beams from the HeNe lasers. Laser line optical bandpass filters attached to the PSD cameras remove unwanted reflected light from the xenon lamp. The computer converts the detector output to the actual sample position.

Sample heating is provided by a 1 kW UV-rich high-pressure xenon arc lamp (ILC, model LX 1000CF). The radiation produced by the bulb is roughly collimated into a 5 cm beam by a parabolic reflector at the back of the bulb housing. The beam is then focused by a 7.5 cm focal length fused quartz lens into a small spot in order to maximize the light flux on the sample. Since the beam originates from a finite discharge gap between the anode and the cathode and not from a point source, the focused spot size could not be reduced to less than 5 mm. Fused quartz was used in order to transmit the UV component of the xenon beam for sample charging via the photoelectric effect. (Sample charging by UV will be described in Sec. V.) A fused quartz mirror, 7.5 cm both in diameter and in radius of curvature, is placed opposite the lens. This mirror collects most of the xenon light beam that misses the sample. The temperature of a 2.5 mm diam zirconium sphere could be varied from room temperature to 2270 K by adjusting the iris in front of the xenon lamp. Without the mirror, the maximum temperature did not exceed 1750 K.

The sample temperature was measured using a custom-built single-color pyrometer which was constructed and calibrated according to the prescription provided by Hofmeister et al.[8] The pyrometer collects the radiative power emitted by a well-defined area on the sample surface into a certain solid angle and over a small wavelength range (10 nm bandwidth at 658 nm wavelength). The collected power can be converted to sample temperature through Planck's equation for the spectral distribution



FLOW CHART OF THE SOFTWARE    (A) FOREGROUND TASK    (B) BACKGROUND TASK
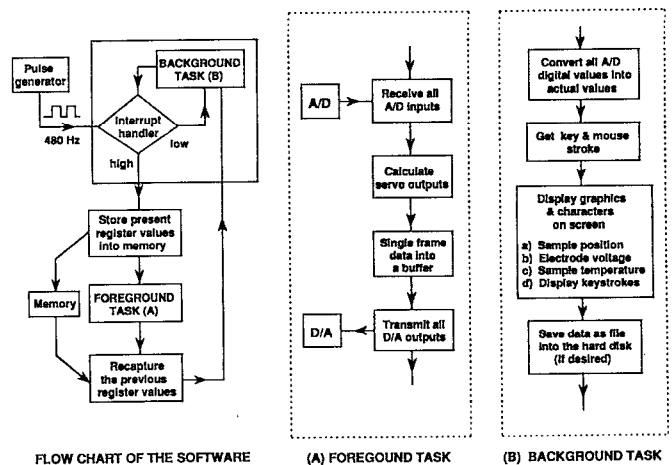
FIG. 4. Flowchart of the position control software.

of emissive power if the pyrometer output corresponding to one temperature, typically the sample's melting point, is known. For zirconium, the rapid increase in temperature to the melting point as a result of recalescence provides an easily recognized reference point, allowing the temperature to be calculated *a posteriori* for the entire undercooling experiment. Data acquisition was by a Macintosh II computer with a National Instruments A/D converter. The driving software automatically recognizes the reference temperature $T_{\text{ref}}$ by searching for the rapid increase in the pyrometer output associated with recalescence. It then calculates the temperature for the entire experiment and provides a plot of temperature versus time. The percentage of undercooling and other important parameters are also computed and displayed.

A close-up view of the sample was videotaped during the experiments using a camera with a telephoto lens.

## IV. THE POSITION CONTROL SOFTWARE

The architecture of the position control software is shown in Fig. 4 in a flowchart format. Software tasks are divided into two groups: FOREGROUND and BACKGROUND. The foreground tasks consist of the servo control and the data collection that require real-time operation. The background tasks consist of a user interface, inputs such as a keyboard and a mouse, and graphics, which are given secondary priority. Data files can also be created and saved onto the hard drive through the background mode. These two modes of operation use the interrupt request capability of the Macintosh computer. When an interrupt signal is issued (from an external programmable pulse generator) the computer sets aside background routines, stores the present state of its registers into memory, and launches the foreground routine. During the foreground routine, the position information is collected from an A/D, the control algorithm is computed, a proper servo control value is sent out through a D/A, and a single frame of data is collected in a specified memory buffer. After the foreground routine is successfully executed, the computer recaptures its previous register values and continues with

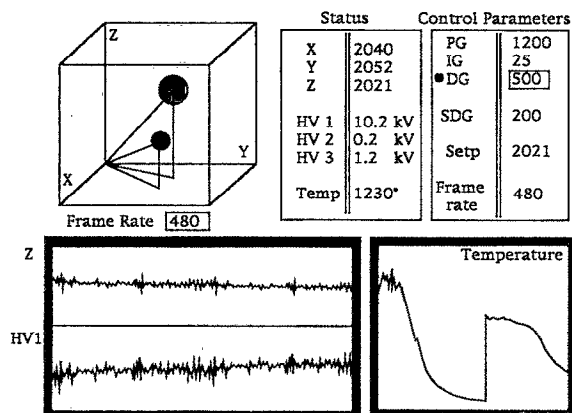| | Status | | Control Parameters | |
|---|---|---|---|---|
| X | 2040 | PG | 1200 | |
| Y | 2052 | IG | 25 | |
| Z | 2021 | ●DG | 500 | |
| HV 1 | 10.2 kV | SDG | 200 | |
| HV 2 | 0.2 kV | | | |
| HV 3 | 1.2 kV | Setp | 2021 | |
| Temp | 1230° | Frame rate | 480 | |

Frame Rate  480

FIG. 5. User interface display used in the present levitator. The cubical box represents the space between the electrodes in which the sample (the gray dot) moves in search of the set point (the black dot) by feedback control. The status column displays the sample position, applied high voltages, and the sample temperature. The control parameter column shows the control parameter inputs. The sample position, the control voltage, and the sample temperature are also displayed in the form of oscillograms.

its background task. This process is set into a continuous loop with an interrupt frequency of 480 Hz.

## A. Servo control

The vertical axis servo control uses a PID (proportional, integral, derivative) algorithm.[9] The $z$-direction output at the $i$th cycle, $O_i$, has the following form:

$$O_i = PG \times e_i + IG \times \sum_{j=0}^{i} e_j + DG \times (e_i - e_{i-1}), \qquad (2)$$

where $e_i = sp - z_i$, error signal at the $i$th loop, $z_i =$ current vertical position, $sp =$ set position, $PG =$ proportional gain, $IG =$ integral gain, and $DG =$ derivative gain. Since the horizontal plane has a passive potential minimum it does not normally require an active feedback control. However, in vacuum, there is no gas medium to damp out horizontal oscillations, so we used a horizontal damping control consisting of two sets of side electrodes. The lateral damping was controlled by the following simple algorithm:

$$O_{ij} = DG \times (e_{ij} - e_{i-1,j}), \qquad (3)$$

where $e_{ij} = sp_j - p_{ij}$, error signal for a single loop, $j = x$ or $y$ component of position, $p_{ij} = x$ or $y$ position at the $i$th cycle. The vertical control is executed in every loop, whereas the horizontal control is executed every tenth loop. The stability of the sample has been found to depend strongly on the vibration of the system originating from floor vibrations. A stability better than 20 $\mu$m was achieved for a 3 mm sample with a specific density of 8, carrying a constant charge.

## B. User interface

The user interface consists of keyboard/mouse inputs and a graphics display. The keyboard/mouse is used for entering servo and other necessary parameters for proper data acquisition. It can, therefore, interrupt the loop at any

time, although the servoloop has a high priority. The graphics display consists of sample positions, control voltage outputs, and temperature readings (Fig. 5). The programs were written in the "C" language except for the interrupt handler routine which was written in assembly code.

## V. SAMPLE CHARGING

Sample charging is a critical part of electrostatic positioning. The amount of charge on the sample surface determines the positioning force on the sample from a given electrostatic field. In order for the electrostatic positioning technique to be employed, the physical processes that allow charges to accumulate on the sample had to be identified. Three charging methods that are relevant during different phases of processing have been employed: capacitive, photoelectric and thermionic charging.

Capacitive charging is employed for sample launching and levitation at the beginning of each experiment prior to the use of the other charging mechanisms. In capacitive charging, surface charge on the sample increases as the top-electrode potential increases until electrical contact with the bottom electrode is broken and the sample is levitated. In order to make the charge polarity consistent with that induced by the other charging methods, a positive charge is induced by applying negative voltages on the top electrode. The initial sample charge will remain unchanged only in the absence of any discharging ions which may be produced by the sample and the surrounding electrodes under strong UV irradiation. When several charging mechanisms are acting simultaneously, sample charging becomes a dynamic process. Photoelectric charging induced by an appropriate UV source will maintain a sufficient charge even in the presence of neutralizing ions. Once the sample temperature exceeds approximately 1200 °C, the more powerful thermionic charging mechanism eventually dominates photoelectric charging, enhancing the sample charge.

Photoelectric emission arises from electron excitation by radiation, usually within a depth that the radiation can penetrate. Emission of a photoelectrically excited electron can occur only if it possesses sufficient energy to reach the surface and overcome the work function. The magnitude of sample charging depends on the photoelectric yield, which is the number of emitted electrons per absorbed photon. For most metals, emission is more effective in the UV range (less than 400 nm). At photon energies of several eV above threshold, the photoelectric yield from metals is of the order of $10^{-4}$ electrons per photon. At photon energies 5–20 eV above threshold (corresponding to wavelengths in the vacuum UV region), the yield increases to a maximum of about 0.1 electrons per photon which is attributed to emissions from the bulk material deep inside the surface layer.[10] Since maintaining a high positive charge on the sample is the objective, it is desirable to encourage high electron emission by the sample while discouraging electron emission by the electrodes. The electrode material should therefore have a higher work function that the sample material.
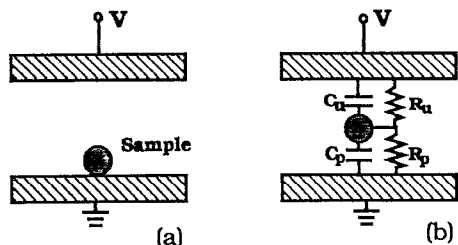
FIG. 6. (a) Electrode and sample arrangements used in the numerical modeling of the initial "cold" levitation. (b) The equivalent $R$-$C$ circuit which was used to model the dynamic sample charging process under UV irradiation.

The rate of thermal electron emission from a heated solid follows the Richardson–Dushman equation:[11]

$$J(\phi_s,T)=AT^2\exp\left(-\frac{\phi_s}{kT}\right),\qquad(4)$$

where $A=120$ A/cm$^2$ K$^2$ (this is the theoretical value and real materials usually have lower values), $k$ is the Boltzmann constant, $T$ is the absolute temperature, and $\phi_s$ is the effective work function. $J$ is a rapidly increasing function of temperature and thermionic emission is the dominant charging mechanism when the sample temperature exceeds 1200 °C, even in the presence of various discharging electrons and ions.

## A. Numerical analysis of capacitive charging

A general-purpose three-dimensional computer model was created to determine the potential, charge, and force distributions on a sample in an electrostatic levitator. Since an analytical solution of this system with arbitrary sample and electrode geometries is impractical, this model uses a numerical finite-difference approach. The potential and charge distributions are obtained using a multigrid method solver[12] and the forces on the sample are derived from these distributions. This model allows us to evaluate and optimize different electrode configurations for the levitator.

The relationships between the parameters (e.g., sample size, position, density, charge, forces, and electrode potentials) that are obtained from this model are shown in Figs. 7–9 to give some insights into this system. In all of the examples the levitator consists of circular top and bottom disk electrodes, separated by 8 mm with the top electrode connected to a HV amplifier and the bottom electrode grounded. The sample was assumed to be spherical [see Fig. 6(a)]. Without going into the details (a detailed description of this model will be published elsewhere), we will simply present a few examples to elucidate the general relationship between sample size, position, density, charge, and electrode voltage.

Figure 7(a) shows the top-electrode potential as a function of sample density and diameter at the moment of launch. The corresponding induced charge on the sample is shown in Fig. 7(b). The top-electrode potential needed to levitate the sample midway between the electrodes is presented in Fig. 8, where the sample is assumed to have retained the charge acquired at launch. Figure 9 shows the
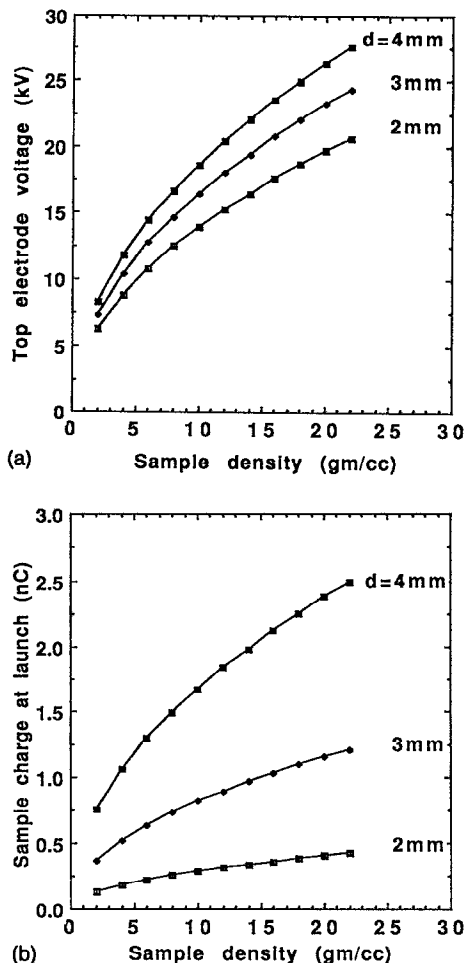


FIG. 7. (a) Top-electrode voltage at the moment of launch vs sample density at three sample diameters. Separation between the top and bottom electrodes is 8 mm. (b) Sample charge at the moment of launch vs sample density at three sample diameters.
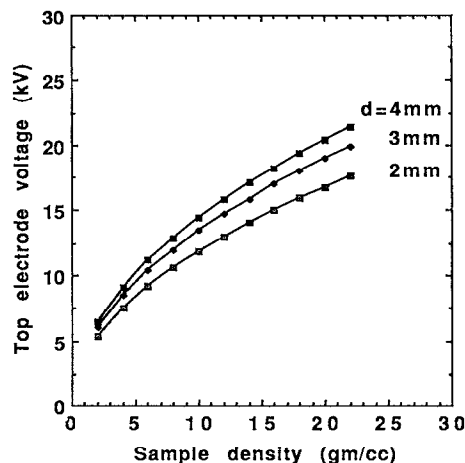


FIG. 8. Top-electrode voltage needed to levitate the sample midway between the electrodes. The sample charge is assumed to be the same as at launch.
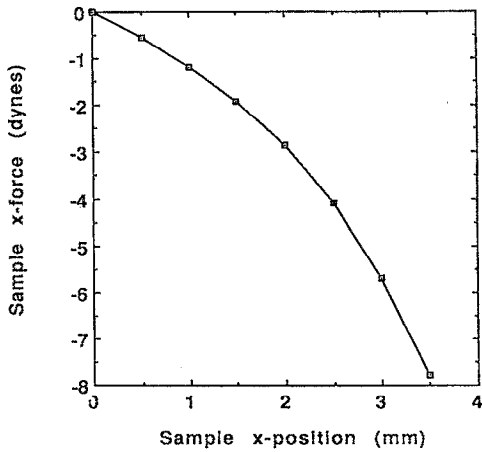
FIG. 9. Sample force in the $x$ axis vs sample position in the $x$ axis with a sample charge of 1.0 nC and a top-electrode voltage of $-10$ kV. Separation between top and bottom electrodes is 8 mm and the sample diameter is 3 mm.

radial restoring force on the sample as a function of sample displacement from the center, which is primarily due to image charges.

## B. A model for sample charging by photoelectric and thermionic emission

When a cold sample is launched with initial charge $Q_s$, it requires a levitation voltage given approximately by Eq. (1). However, $V$ and $Q_s$ change when the sample is irradiated by UV or when the sample temperature is high enough to cause thermionic emission. When the sample is heated by a focused xenon lamp, the UV component ejects electrons not only from the sample but also from surrounding materials as a result of reflection and scattering. The equilibrium charge of a levitated sample is established through the balance of electrical currents flowing between the sample and electrodes. These include photoelectric and thermionic currents, as well as currents resulting from ionization of gases and other volatile materials. Consider the case in which the sample has reached a steady-state temperature and is positioned between the top electrode (at a negative potential $V$) and the bottom electrode (grounded). A current $I_p$ (taken to be positive for electrons leaving the sample) flowing from the sample to the bottom electrode may be expressed by

$$I_p = -\alpha_s V_s \left[ Y_s f_s F + \delta_s + J(\phi_s, T_s) \right] \equiv -V_s/R_p, \quad (5)$$

where $\alpha_s$ is a geometrical factor relating relative sizes and shapes of the sample and electrode to the amount of current that can be extracted from the sample at a given sample potential $V_s$, $Y_s$ is the sample's photoelectric yield, $f_s$ is the fraction of the xenon lamp flux which has photon energy larger than the sample's work function, $F$ is the total xenon lamp flux falling on the sample, $\delta_s$ represents positive ionization of gas molecules on the sample's lower surface via surface ionization (Ref. 13), $J(\phi_s, T_s)$ is the thermionic current as defined in Eq. (4), and $R_p$ is defined as the equivalent resistance at a given operating point. Simi-

larly, the current flowing from the top electrode to the sample (taken to be positive for electrons leaving the top electrode) is

$$I_u = \alpha_u (V_s - V)(Y_u r_s s_{su} f_u F + \delta_u) \equiv (V_s - V)/R_u, \quad (6)$$

where $\alpha_u$ is a geometrical factor relating the sample and electrode shapes to the amount of current which originates from the top electrode at potential $V$ and reaches the sample, $Y_u$ is the top electrode's photoelectric yield, $r_s$ is the sample reflectivity, $s_{su}$ is the fraction of the reflected beam falling on the top electrode, $f_u$ is the fraction of the xenon lamp output which has energy higher than the top electrode work function, $\delta_u$ represents positive ionization of gas molecules on the sample's lower surface, and $R_u$ is defined as the equivalent resistance at a given operating point. The present situation may be represented by an equivalent circuit shown in Fig. 6(b) where $C_u$ and $C_p$ are the mutual capacitances between the sample and the top and the bottom electrodes, respectively. Therefore, the sample charge is given by

$$Q_s = Q_p - Q_u$$
$$= C_p V_s - C_u (V - V_s)$$
$$= (C_p + C_u) V_s - C_u V, \quad (7)$$

where $Q_p$ is the charge on $C_p$, and $Q_u$ is the charge on $C_u$.

If the top-electrode voltage jumps from an initial steady-state value $V_0$ to a final value $V_f$, then the solutions of the equivalent circuit are given by

$$V_s(t) - V_{s0} = [V_s(\infty) - V_{s0}][1 - \exp(-t/\tau)], \quad (8)$$

where

$$V_s(\infty) = V_f \frac{\alpha}{1+\alpha}, \quad (9)$$

$$\tau = (C_p + C_u) R_p/(1+\alpha), \quad (10)$$

with

$$\alpha \equiv R_p/R_u = \frac{\alpha_u (Y_u r_s s_{su} f_u F + \delta_u)}{\alpha_s [Y_s f_s F + \delta_s + J(\phi_s, T_s)]}, \quad (11)$$

where Eq. (11) results from Eqs. (5) and (6). The solution for the sample charge, $Q_s(t)$, takes the same form as Eq. (8) with the same $\tau$ given by Eq. (10):

$$Q_s(t) - Q_{s0} = [Q_s(\infty) - Q_{s0}][1 - \exp(-t/\tau)], \quad (12)$$

where

$$Q_s(\infty) = -V_f \frac{C_u - \alpha C_p}{1+\alpha}. \quad (13)$$

Since $V_{s0}$ and $Q_{s0}$ are also steady-state values their expressions are given by Eqs. (9) and (13), respectively, with $V_0$ replacing $V_f$.

If a spherical sample is midway between the electrodes, then $C_p \approx C_u \equiv C$, and $C$ will be proportional to the sample surface area. Assuming $V_{s0} = 0$ so that $Q_{s0} = 0$, we have

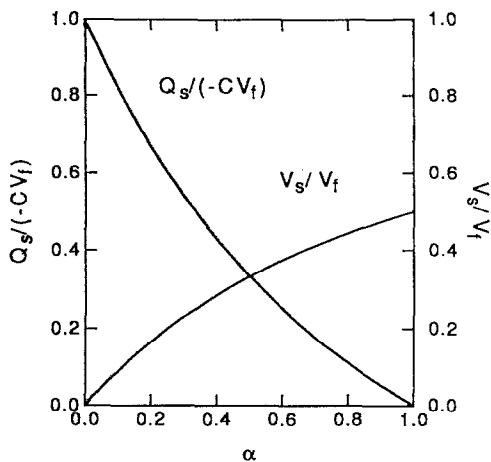$$V_s(\infty) = V_f \frac{\alpha}{1+\alpha}, \quad (14)$$

FIG. 10. Sample charge and sample voltage vs $\alpha$ when a fixed voltage $V_f$ is applied to the top electrode.

$$Q_s(\infty) = -V_f C \frac{1-\alpha}{1+\alpha}. \tag{15}$$

From Eqs. (1), (12), and (13), the force exerted on the sample is

$$F_{es}(t) = -\frac{V_f^2 C(1-\alpha)}{L(1+\alpha)}[1-\exp(-t/\tau)] \tag{16}$$

and from Eq. (10),

$$\tau = \frac{2CR_p}{1+\alpha}. \tag{17}$$

From these equations the following observations can be made:

(i) Since $\alpha$ is defined as a positive number in Eq. (11), the maximum positive sample charge cannot exceed $-V_f C$ and it can completely disappear when $\alpha=1$. Dependence of $Q_s(\infty)$ and $V_s(\infty)$ on $\alpha$ can be seen more clearly in Fig. 10. In order to maintain a sufficient charge for levitation, one must control the parameters in Eq. (11) so that $\alpha$ is sufficiently small.

(ii) Since the sample charge is linearly dependent on $V_f$, $F_{es}(\infty)$ should show quadratic dependence on $V_f$ as in Eq. (16). This was experimentally verified as shown in Fig. 11. The force exerted on the sample in a UV-rich environment was measured as a function of the electrode voltage using a dynamic balance. Of course, according to Eq. (16), the magnitude of the parabola appearing in Fig. 11 is determined by $\alpha$, $L$, and $C$.

(iii) In order to achieve a fast response time, according to Eq. (17), $CR_p$ should decrease, that is, since $C$ is fixed for a given sample, $R_p$ should decrease. This may be accomplished [Eq. (5)] by increasing the lamp flux $F$, and eventually by increasing $J(\phi_s, T_s)$ at higher temperatures. This trend was verified experimentally, again using the dynamic balance, as shown in Fig. 12. When the sample reached a steady state under a certain UV flux, a $-10$ kV step was applied to the electrode and the force imparted on the sample was recorded. As Fig. 12 shows, the basic trend is in accordance with Eq. (16).
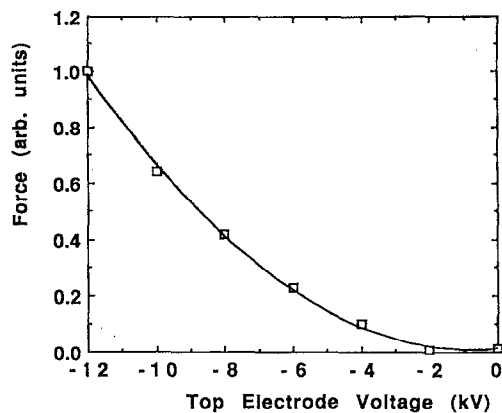


FIG. 11. The electrostatic force on the sample as a function of applied voltage on the top electrode.

(iv) If the sample is levitated using a top-electrode voltage $V_f$, then, from Eqs. (1) and (15), one obtains the sample charge and the required levitation voltage:

$$Q_s(\infty)^2 = mgLC\frac{1-\alpha}{1+\alpha} \tag{18}$$

and

$$V_f^2 = \frac{mgL}{C}\frac{1+\alpha}{1-\alpha}. \tag{19}$$

Figure 13 shows that sample charge holds its largest value, $\sqrt{mgLC}$, when $\alpha=0$, requiring the lowest electrode voltage, and the sample holds no charge if $\alpha=1$.

(v) We have seen from above examples the important role $\alpha$ plays in sample charging, and for levitation we prefer $\alpha \ll 1$. From Eq. (11),

$$\alpha_u(Y_u r_s s_{su} f_u F + \delta_u) \ll \alpha_s[Y_s f_s F + \delta_s + J(\phi_s, T_s)].$$

In the thermionic temperature region where $J(\phi_s, T_s)$ dominates the other terms this inequality can be easily
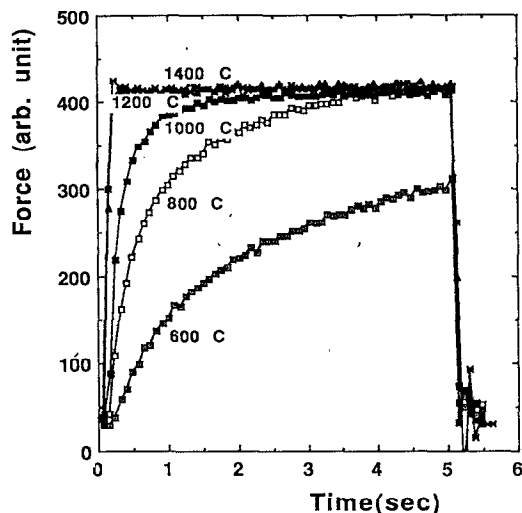


FIG. 12. The transient behavior of the electrostatic force as a result of the application of a $-10$ kV step at different UV flux and sample temperatures.
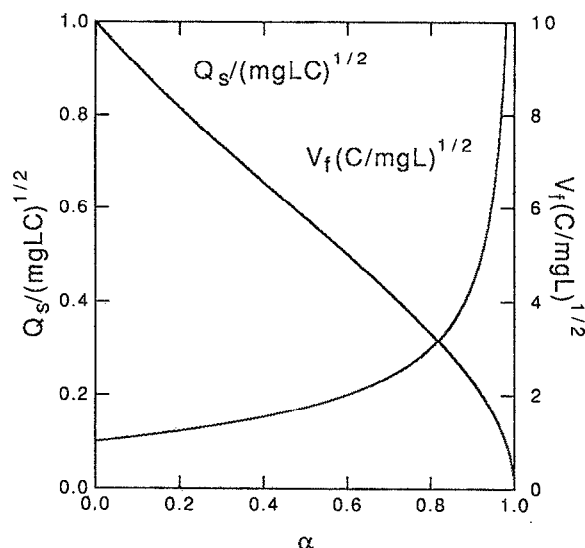
FIG. 13. Sample charge and corresponding levitation voltage vs $\alpha$ while the sample is levitated against the gravitational force.

satisfied unless $\delta_u$ is equally high. In actual experiments we have observed more quiescent sample levitation with a large sample charge as soon as the temperature exceeded about 1200 °C. Therefore, the major concern for sample levitation may arise in the lower temperature range where $J(\phi_s, T_s)$ is insignificant. Since $0 \geqslant V_s > V_f$, a neutral atom ionized near the top surface of the sample donates an electron to the sample, while the positive ion strikes the top electrode, producing electrons which will shower onto the sample, further decreasing the charge, i.e., increasing $\delta_u$. On the other hand, a positive ion produced at the bottom surface of the sample cannot escape the sample due to the opposing field condition, thus ensuring $\delta_s \ll \delta_u$. Therefore, the issue is whether one can control the remaining parameters in such a way that

$$\alpha_u (Y_u\, r_s\, s_{su}\, f_u F + \delta_u) \ll \alpha_s\, Y_s\, f_s\, F.$$

For a fixed xenon lamp flux $F$, the condition $f_u \ll f_s$ can be achieved by choosing the work function of the top electrode larger than that of the sample, the condition $r_s \ll 1$ may be satisfied if the sample surface is not highly reflecting, and the situation $s_{su} \ll 1$ can be provided by making the solid angle extending to the electrode from the sample as small as possible. If the effect of $\delta_u$ cannot be easily overcome, the only remaining remedy might be to reduce $\delta_u$ itself by allowing more gradual outgassing as the sample temperature is raised more slowly.

## VI. SAMPLE PREPARATION

Clean, spherical samples of various metals were prepared for the undercooling experiments using a chemical etch and thermal outgassing treatment. The procedure was as follows: A rod made from the metal of interest was machined with a neck and bulb at one end. A chemical degrease and etch was applied to the rod to remove organic and inorganic surface impurities. The chemical treatment depended on the rod's composition. For all metals the first step involved degreasing in trichloroethylene and in acetone each for 1 min. The second step consisted of a chemical etch of the surface to remove the oxide layer and other inorganic surface impurities. The optimum acid etch solutions for many metals can be found in Ref. 14.

After cleaning and etching, the rod was mounted vertically with the bulb facing down in a sample preparation chamber evacuated to $\sim 10^{-7}$ Torr. The bulb was heated by electron bombardment from a heated tungsten filament coil. About 4 kV potential was applied between the filament and the grounded rod. The bulb was kept just below its melting temperature for several hours to allow any adsorbed and absorbed gases to outgas. The heating was then increased until the bulb melted and formed a spherical pendant drop at the end of the rod. The heating was then terminated and the drop was allowed to cool and solidify. The chamber was purged with dry argon gas and the sample was clipped from the rod, ready for use in undercooling experiments. The size of the resulting sample could be easily controlled by the size of the initial bulb at the end of the rod.

## VII. OPERATING PROCEDURE AND SYSTEM PERFORMANCE

The sample was positioned on the bottom electrode and the chamber evacuated $\sim 10^{-8}$ Torr. The position control software was turned on and the appropriate set position and PG, DG, and IG gains were keyed in. A Trek 20 kV amplifier (model 620A) was used for the $z$-axis control and two Trek 10 kV amplifiers (model 609A) were used for the $x$- and $y$-axis damping. As soon as the top electrode reached the threshold voltage the sample jumped away from the bottom electrode towards the set position. Minor adjustments to the gains and set point were then made to establish the most quiescent levitation conditions. The stability was typically better than 20 $\mu$m at this point.

The iris in front of the xenon lamp was then opened gradually while the levitation voltage was being monitored. Changes in the sample charge are manifested by corresponding changes in the levitation voltage according to Eq. (1). If a substantial charge decrease occurred, the iris was adjusted so that the required control voltage remained within the range of the high-voltage amplifiers ($\pm 20$ kV in this case). Ion production at the sample surface seemed to depend on the cleanliness of the sample surface and the degree of outgassing. Since the impurities outgassed during heating may be ionized and reduce the sample's charge, the impurities that are volatile at each temperature are removed through gradual heating of the sample and this process is continued until the desired final temperature is reached. As discussed above, since the sample charge is determined by $\alpha (= R_p/R_u)$ in the equivalent circuit [Fig. 6(b)], enough charge may be maintained by making $\alpha$ sufficiently small, i.e., by reducing $R_p$ with increased photoemission current while maintaining $R_u$ relatively unchanged. A top electrode having a higher work function than the sample is generally preferred. A 2.5 cm diam gold plated copper mirror used as an electrode performed well in the present system. As the sample charge changed dur-
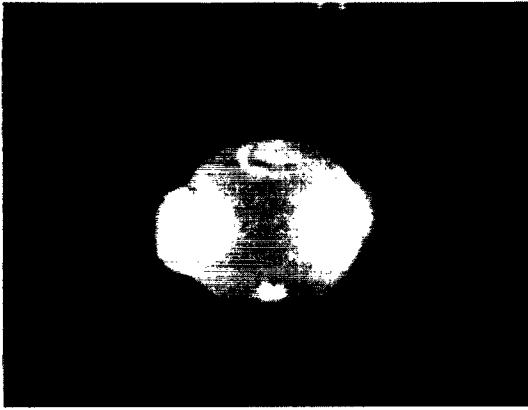
Electrostatic levitator

FIG. 14. A molten zirconium sample being levitated at 2250 K.



FIG. 15. Temperature vs time as a superheated zirconium drop undergoes radiative cooling.

ing heating, the control gains were frequently adjusted in order to maintain the best position stability.

## VIII. DEMONSTRATION OF AN UNDERCOOLING EXPERIMENT

Once the sample melted and reached the desired superheated temperature, it was ready for an undercooling experiment. In a vacuum environment the change in enthalpy of the sample is equal to the difference between the heat arriving from the xenon beam and that lost due to radiation

$$\rho V C_p \, dT/dt = Q_{in} - A\sigma\epsilon_T (T^4 - T_b^4), \qquad (20)$$

where $\rho$ is the sample density, $V$ is the volume, $C_p$ is the heat capacity, $Q_{in}$ is the heat due to the beam, $A$ is the sample surface area, $\sigma$ is the Stefan–Boltzmann constant, $\epsilon_T$ is the total hemispherical emissivity, $T$ is the sample temperature, and $T_b$ is the background temperature. This formulation assumes that the background acts as a blackbody, which is true in most cases where the chamber is much larger than the sample. We have neglected in Eq. (20) the heat conducted away by the surrounding gas. An estimation showed that, at $p = 10^{-6}$ Torr and $T = 490$ K, the conductive cooling rate is only 5% of the radiative cooling. At higher temperatures the radiative cooling becomes even more dominant. The steady-state temperature $T_f$ is then given by

$$T_f = (Q_{in}/A\sigma\epsilon + T_b^4)^{1/4}. \qquad (21)$$

If the xenon beam is turned off, then $Q_{in} = 0$ in Eq. (20), and $T_f$ will decay to $T_b$ due to radiative cooling. Figure 14 shows a molten drop of zirconium (density 6.49 g/cm³) being levitated at $T_f = 2250$ K (120 K above its melting temperature) in the presence of a heating beam. The sample diameter was approximately 2.5 mm. The highlight spots seen on the sample disappeared when the beam was turned off. Figure 15 shows a temperature versus time curve of the same sample when the heating beam was suddenly removed at the sample temperature of 2250 K. Before the beam was removed the pyrometer was strongly influenced by reflected radiation, showing a high level of noise as seen at the beginning of the curve. Therefore, the
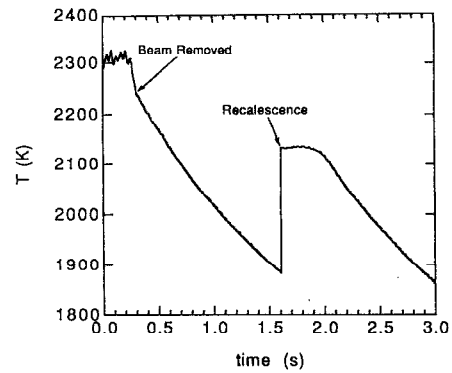
temperature reading is inaccurate while the lamp is on. As soon as the beam is blocked the sample underwent radiative cooling according to Eq. (20) (with $Q_{in} = 0$) until recalescence occurred. Recalescence is marked by a sudden increase in temperature to its melting point as the sample releases its latent heat. The liquid–solid phase transition period lasted for approximately 0.3 s before the sample temperature decayed again. The data presented in this figure was obtained by digitizing the pyrometer output at 1 kHz.

Since $(T/T_b)^4 > 10^3$ during the undercooling period, one can integrate Eq. (20), assuming $T_b \approx 0$ and $\rho V C_p / 3A\sigma\epsilon_T \approx$ const, to give

$$t - t_0 = (\rho V C_p / 3A\sigma\epsilon_T)(T_0^{-3} - T^{-3}), \qquad (22)$$

where $T_0$ is the sample temperature at $t = t_0$. A plot of $t$ vs $T^{-3}$ is shown in Fig. 16 confirming a linear relationship.

The ESL allows convenient repetition of the superheating-undercooling-recalescence cycle. This allowed the undercooling temperature for the same 2.3 mm sample of zirconium to be measured for over 100 cycles in about two hours. Figure 17 shows the normalized cumulative distribution of nucleation events $(n_e/N_T)$ versus the percentage of undercooling.
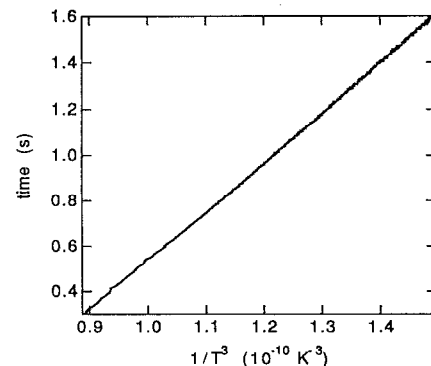


FIG. 16. Time vs $T^{-3}$ of the undercooling segment (between 0.3 and 1.6 s) shown in Fig. 15.
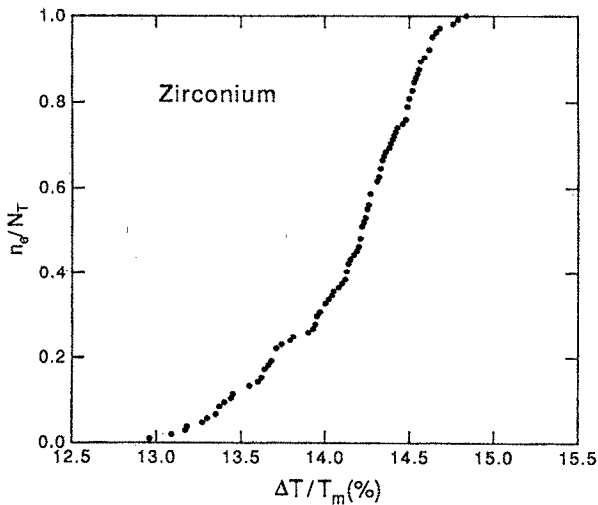
FIG. 17. Normalized cumulative distribution function vs percentage of undercooling for a 2.3 mm diam sample of zirconium.

## IX. DISCUSSION

We have described some of the basic principles and physical mechanisms involving a high-temperature electrostatic levitator operated in vacuum in the presence of gravity. The basic PID feedback routine seems to be adequate for position control despite the fact that the sample charge was subjected to a dynamic process. Rapid advancements in some commercial products, notably the high resolution position detector, the high-speed microcomputer, the high-voltage amplifiers, the vibration-free vacuum pumps, and user friendly programming languages, have greatly improved the system performance and made the construction of a new system easier.

So far we have successfully melted and solidified numerous sample materials (melting temperatures are shown in parentheses) such as In (157 °C), Sn (232 °C), Bi (271.44 °C), Pb (327 °C), In 0.69 w % Sb (492.5 °C), Al (670 °C), Ge (938 °C), Cu (1083 °C), Ni (1455 °C), and Zr (1855 °C). In the case of zirconium we have completed more than 400 quantitative undercooling experiments. Results of these experiments will be published elsewhere. We have also demonstrated the capability to process nonconducting sample materials, an area which we plan to investigate further in the near future.

The simple resistance-capacitance ($R$-$C$) circuit used to model the charge gain/loss behavior under the influence of photoelectric or thermionic emission may be an oversimplification. However, the present model has been very useful for identifying those physical mechanisms which affect the sample charge. Constructing a more realistic model will be possible as we gain more experience with the system. A systematic experimental investigation is being

planned. One important practical lesson we have learned is that in order to conduct a successful experiment one must begin with a clean sample (with reduced volatile contents) and heat it slowly until it reaches thermionic temperatures.

The levitator described in this article is primarily for Earth-based applications. It can, however, be readily converted for operation in a reduced-g environment. First we note that the sample charge produced by photoelectric and thermionic emissions is positive and proportional to the magnitude of the applied field, therefore, the control force is proportional to $V^2$ in magnitude and opposed to the applied field. The isotropic force environment of space leads to an electrode assembly having a tetrahedral symmetry with four spherical electrodes.[1] The design of a system specifically for space application is underway and will be described elsewhere.

## ACKNOWLEDGMENTS

[1] W. K. Rhim, M. Collender, M. T. Hyson, W. T. Simms, and D. D. Elleman, Rev. Sci. Instrum. **56**, 307 (1985).

[2] P. J. Wyatt and D. T. Phillips, J. Colloid. Interface Sci. **39**, 125 (1972).

[3] S. Arnold, J. Aerosol Sci. **10**, 49 (1979); L. Altwegg, M. Pope, S. Arnold, W. Y. Fowlkes, and M. A. El Hamamsy, Rev. Sci. Instrum. **53**, 332 (1982).

[4] M. R. Libera, P. P. Bolsaitis, R. E. Spjut, and J. B. VanderSande, J. Mater. Res. **3**, 441 (1988); E. Bar-Ziv, D. B. Jones, R. E. Spjut, D. R. Dudek, A. F. Sarofim, and J. P. Longwell, Combust. Flame **75**, 81 (1989).

[5] C. A. Hahs and R. J. Fox, Proceedings of the 4th International Conference on Experimental Methods for Microgravity Materials Science Research, edited by R. A. Schiffman (Warrendale, PA, 1992), p. 23.

[6] For Earnshaw's theorem, see, for example, S. A. Stratton, *Electromagnetic Theory* (McGraw-Hill, New York, 1941), p. 116.

[7] W. K. Rhim, S. K. Chung, E. H. Trinh, and D. D. Elleman, Proc. Mater. Res. Soc. **87**, 329 (1987).

[8] W. F. Hofmeister, R. J. Bayuzick, and M. B. Robinson, Rev. Sci. Instrum. **61**, 2220 (1990).

[9] J. A. Cadzow and H. R. Martnes, *Discrete Time and Computer Control Systems* (Prentice-Hall, Englewood Cliffs, NJ, 1970).

[10] R. Gomer, *Field Emission and Field Ionization* (Harvard University, Cambridge, MA, 1961).

[11] A. J. Dekker, *Solid State Physics* (Prentice-Hall, Englewood Cliffs, NJ, 1962), p. 221.

[12] Achi Brandt, *Multigrid Techniques: 1984 Guide*, Lecture notes for Computational Fluid Dynamics Lecture Series, Rhode-Saint-Genese, Belgium, 26–30 March 1984; W. L. Briggs, *A Multigrid Tutorial* (Society for Industrial and Applied Mathematics, Philadelphia, PA, 1987).

[13] E. Ya. Zandberg and N. I. Ionov, Sov. Phys. Usp. **67**, 255 (1959).

[14] R. C. Snogren, *Handbook of Surface Preparation* (Palmerton, New York, 1974).